Supplementary Information

1. Dataset and methods

1.1 Airborne datasets

The canopy reflectance for full-spectrum (i.e., 350~2500 nm with the spectral resolution of 1 nm) was acquired in the NASA HyspIRI Airborne Campaign[1,2]. The reflectance was measured over managed agricultural fields in the Imperial Valley, Central Valley, and other vegetation such as chaparral/shrubland, savanna in Sierra mountain forests in California. There were in total 156 observations measured during spring (March and April) and early summer (June) in 2013 and 2014, and these observations were atmospherically corrected to obtain surface reflectance[1]. The reflectance at 469nm, 648nm and 858nm that fall in the central wavelength of Moderate Resolution Imaging Spectroradiometer (MODIS) surface reflectance in the blue, red and NIR bands was used.

1.2 Satellite datasets

The daily MODIS MCD43A4 V6 Nadir Bidirectional Reflectance Distribution Function (BRDF)-Adjusted Reflectance (NBAR) data[3]; the 4-day MCD15A3H V6 level-4, Combined Fraction of Photosynthetically Active Radiation (FPAR) and Leaf Area Index (LAI) data[4]; and the yearly MCD12Q1 V6 Land Cover Type[5] datasets were used. All MODIS datasets with 500 m spatial resolution were obtained from the Google Earth Engine (GEE) platform[6]. Only snow-free MODIS NBAR and FPAR data with good Quality Assurance (QA) flags were used. The International Geosphere-Biosphere Programme (IGBP) classification layer in the MCD12Q1 data was used to calculate the proportions of each land cover type within a given pixel. The TROPOMI far-red daily SIF dataset with a spatial resolution of 7 km × 3.5 km at nadir[7] from ftp://fluo.gps.caltech.edu/data/tropomi, and DSCOVR/EPIC-derived daily PAR data with 0.1° × 0.1° spatial resolution were used[8,9]. The SIF/PAR ratio can be used to normalize SIF by solar incident irradiance and to be comparable with VIs. The time period of 2018.03-2019.02 was consistent with the TROPOMI SIF dataset, which started in March, 2018. The data were averagely aggregated to 4-days, and the spatial resolution was aggregated to 0.1°. In the spatial aggregation, the red, NIR and blue reflectance was firstly averagely aggregated to 0.1 degrees, and then the VIs were calculated. All pixels with the proportion of non-vegetation types (i.e., snow/ice, water, barren and urban) larger than 50% were excluded in the analysis.

1.3 Radiative transfer model simulations

The comparison between different VIs was first carried out based on the Soil Canopy Observation, Photochemistry and Energy fluxes (SCOPE) v1.70 model[10] simulations at different canopy structure, sun-sensor geometry, soil background and leaf spectral properties. NIR_{BS} represents the NIR reflectance of vegetation with a black soil background. Leaf area index: [0.5, 1, 3, 5]; leaf angle distribution: spherical, erectophile, planophile; leaf chlorophyll content (μg cm^{-2}): [40, 60, 80]; solar zenith angle: [20°, 30°, 40°, 50°, 60°]; view zenith angle: [0°, 10°, 20°, 30°, 40°, 50°, 60°]; soil spectra: four soil spectrum. The broadband incoming shortwave radiation (0.4-2.5 um) was set at 600 W m^{-2} for each simulation, and thus the VIs and SIF are still comparable although they have different units. Default values for SCOPE v1.70 were used for all other parameters, e.g., Vcmax=60 μmol m^{-2} s^{-1}. In accordance with the satellite and airborne data, the simulated reflectance at 469 nm, 648 nm and 858 nm as the blue, red and NIR bands was used to calculate the vegetation indices: NIRv, DVI, EVI and EVI2. The SIF at 760nm was also simulated using the SCOPE model. Then the soil background was replaced with zero reflectance to calculate the NIR_{BS}.

To evaluate the sensitivity of the vegetation indices to different atmosphere conditions, the Second Simulation of a Satellite Signal in the Solar Spectrum (6S) model[11] was used to convert the top-of-canopy reflectance from the SCOPE v1.70 model to the top-of-atmosphere reflectance, for visibility levels of 5 km and 100 km, respectively.

2. Similarity and sensitivity of VIs

Below we discuss the intrinsic features of several widely-used VIs at the global scale, including NDVI, EVI, EVI2 and NIRv, with an emphasis on their response to the artefacts such as the impacts of soil background, atmospheric contamination, canopy structural and sun-target-sensor geometry effects.

2.1 Similarity and difference among VIs

Canopy radiative transfer models and airborne data confirm strong linear correlations between NIRv, DVI, EVI and EVI2 (Figs. S1 and S2). All of them can be good proxies of pure vegetation NIR reflectance, an ideal metric for retrieving vegetation attributes and can be represented by NIR surface reflectance with a black soil background (NIR_{BS})[12], which is considered as a robust indicator of the fraction of absorbed photosynthetically active radiation (FPAR). NIRv is currently the best approximation of NIR_{BS} considering the physical representation and its magnitude. Satellite-based data also confirm that these four widely used VIs show consistent spatio-temporal correlations (Fig. 3; Figs. S3 and S4), with high correlation coefficients (>0.9 in most regions especially over dense canopies at the global scale). Such relationships are also supported by several existing studies[13,14]. Therefore, we could use any of the four VIs for spatio-temporal analyses over densely vegetated areas with strong confidence because they are functionally equivalent and would theoretically yield similar results, while NDVI behaves differently.

2.2 Sensitivity of these VIs

Resistance of VIs to soil and atmospheric impacts varies. SAVI and EVI have been intentionally designed to reduce the influence of soil background based on the soil spectrum line, with a shift of the origin of the reflectance spectra in the red-NIR space to account for the soil-vegetation interactions[15,16], and thus are relatively insensitive to effects of background soils. By contrast, NDVI is more sensitive to soil than SAVI, especially at low fractional vegetation cover[15,17]. NDVI can be expressed as DVI/(NIR+Red). Since DVI is less sensitive to the soil brightness than the single band reflectance, brighter soil may mostly increase the denominator and thus reduce NDVI, while darker soil may mostly decrease the denominator and increase NDVI[18]. Therefore, wet soil with lower reflectance usually leads to a higher NDVI[17]. Similarly, NIRv partially reduces the soil impacts because of the opposite response of NDVI and NIR to the changes of soil brightness, and for example, smaller (or larger) NDVI and larger (or smaller) NIR are expected with brighter (or darker) soil.

By design, EVI achieved considerable improvements for minimizing atmospheric effects[19] compared to NDVI[20]. In fact, EVI is one of the few indices that are resistant to both changing atmospheric conditions (according to a comparison with TOA reflectance data) and soil background (Fig. S5)[16]. Other VIs without a blue band are less robust than EVI under different atmospheric conditions (Fig. S5), although they perform similarly as EVI if atmospheric effects are minimal or properly corrected. However, the atmospherically corrected blue reflectance is usually noisier than that in red and NIR bands due to effects of aerosols, sub-pixel clouds or sub-pixel fractional snow cover[21], which may bring additional uncertainty to practical EVI-based analyses (Fig. S3).

The formula of NDVI can be reorganized as a monotonously increasing function of SR (Eq. 5)[22]. As leaf multiple scattering is much stronger in the NIR band than in the red band, the SR of shaded leaves is relatively larger than that of sunlit leaves, as is the case for NDVI. Nevertheless, the magnitudes of NIR and red reflectance and their differences (DVI) are expected to be smaller in shaded leaves than in sunlit leaves. Therefore, DVI is typically smaller with more canopy shadows in view, while NDVI is the opposite. Radiative transfer model simulations also show that EVI, EVI2, NIRv, and DVI have similar hemispheric distributions with view angle, while NDVI is different (Fig. S6). EVI is the largest in the direction where the sun and view angle coincide (hotspot), and the smallest in the forward scattering direction (dark-spot[23]). In contrast, NDVI gradually changes from its minimum at the hotspot angle to the maximum value at dark-spot (Fig. S6). However, the variation of NDVI due to different view geometries simulated over a homogeneous canopy, of LAI=3, is only about 10% of its nadir value, which is relatively small compared to 30% for EVI and NIRv (Fig. S6).

Therefore, NDVI has been found to be less sensitive to the sun-target-sensor geometry than EVI and NIRv (Fig. S6), and as well as the single-band red and NIR reflectance[24-26]. These differences in sensitivities to view geometries can be understood on the basis of mechanistic reasoning: as the shape of BRDF is more or less similar across adjacent spectral bands (all have hotspot although not the same sharp), the ratio of spectral bands can reduce the sun-target-sensor geometry effects on remote sensing measurements[27]. Therefore, ratio-based VIs such as NDVI, SR and MSR are slightly less sensitive to such artefacts than other VIs such as DVI, EVI, EVI2 and NIRv, although such artefacts are still not negligible as indicated by Eqs. 8 and 9. This has been reported in studies such as the large impacts of the sensor view angle changes in AVHRR datasets in global greening/browning studies[24,28]. PRI, CCI and a few other red-edge VIs are also ratio-based VIs and therefore have similar characteristics as NDVI regarding the sensitivity to view geometry[29-31], while we recommend all the VIs to be angular-corrected by the kernel-driven BRDF model[32] especially in the applications of time-series analysis or the images with different acquisition times and platforms. The degree of robustness to the artefacts due to soil, sun-target-sensor geometry, and atmospheric aerosol impacts of several widely used VIs are summarized in Table 1.

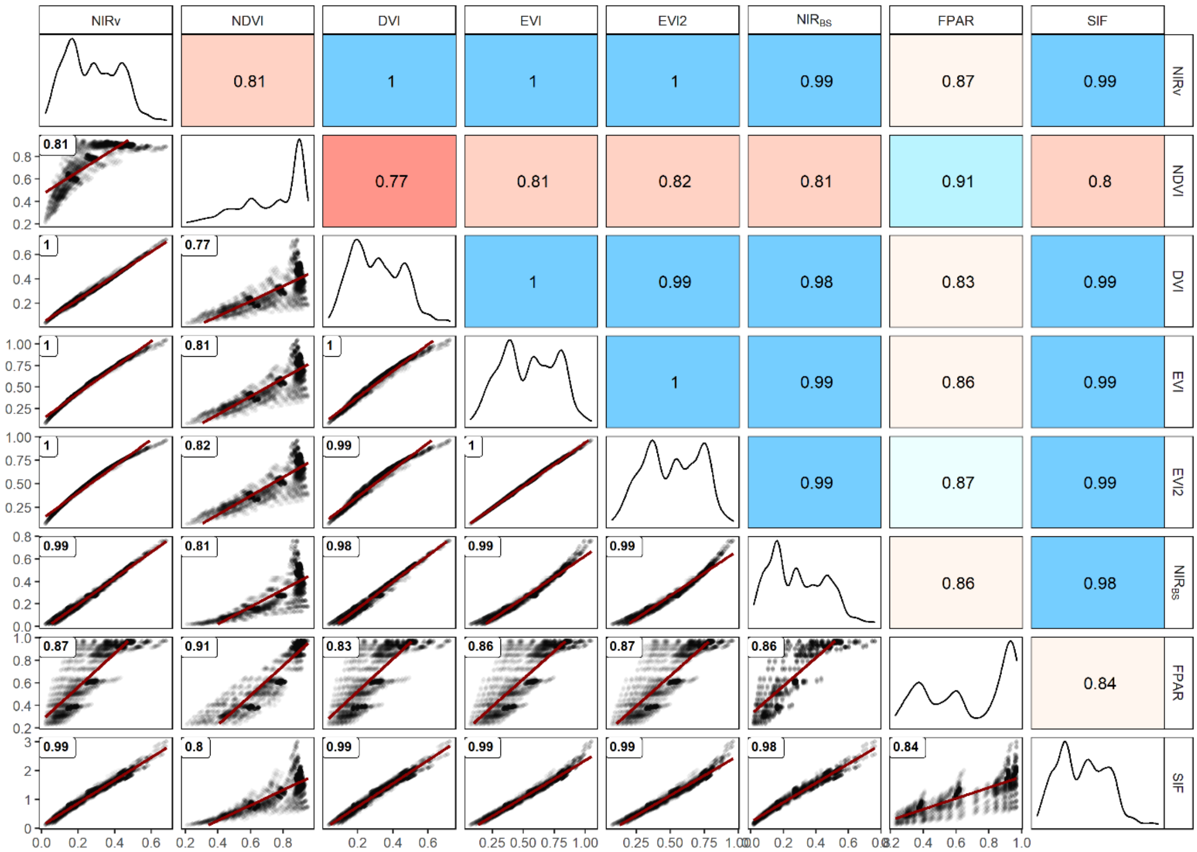

Fig. S1 The comparison among different VIs and SIF based on the SOPE model simulations. The simulation was conducted using a wide range of canopy structure, sun-sensor geometry, soil background and leaf spectral properties. Except for NDVI and FPAR, all the other remote sensing indices: NIR_{BS}, NIRv, DVI, EVI, EVI2 and SIF under no stress conditions, were well correlated with each other, with the correlation coefficient (*R)* greater than 0.97. NIR_{BS} represents the NIR reflectance of vegetation with a black soil background (no soil contribution, or soil reflectance is zero), and can serve as the reference to evaluate the performance of different VIs. There are slight nonlinearities between EVI, EVI2 and NIR_{BS}, NIRv, DVI, as EVI and EVI2 values are smaller for dense vegetation conditions. EVI and DVI are larger than NIR_{BS} for small values, while NIRv was the closest to the origin of coordinates when compared to NIR_{BS}, and the slope of NIRv versus NIR_{BS} was the closest to 1. NIR_{BS} can be best approximated by NIRv with the highest R value, which is important for the photon escape ratio *fesc* calculation. Only NDVI had a different trend than NIRv, EVI and DVI, when compared to NIR_{BS}.

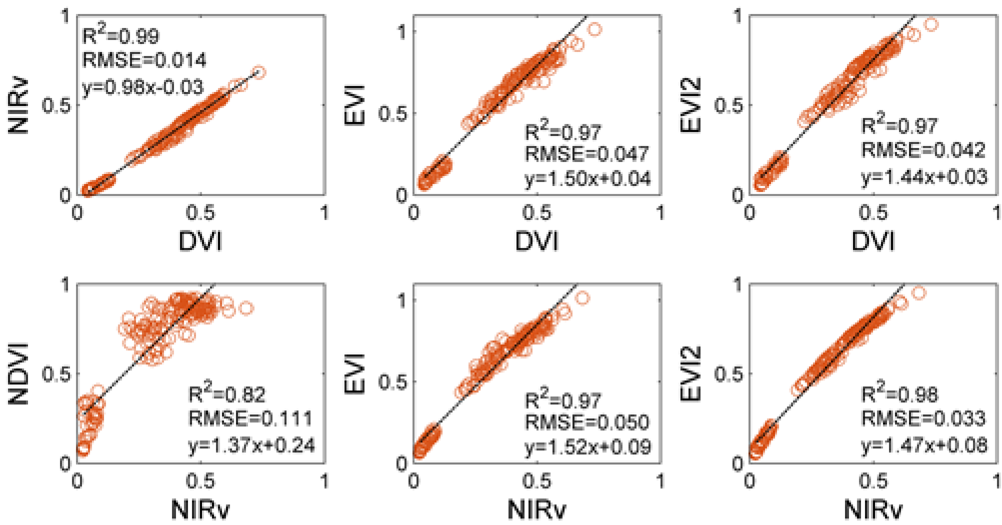

Fig. S2 The comparison between different VIs with DVI and NIRv from NASA HyspIRI Airborne Campaign. The study area is over managed agricultural fields and Sierra mountain forests in California. NIRv, DVI, EVI and EVI2 were well correlated with each other, with the coefficient of determination (R^2) greater than 0.97, although EVI and EVI2 show slight nonlinearity with DVI and NIRv for dense vegetation canopies. NDVI and NIRv have weaker linear relationships and show some nonlinearity, although the R^2 of the linear regression is 0.82 for the airborne datasets.

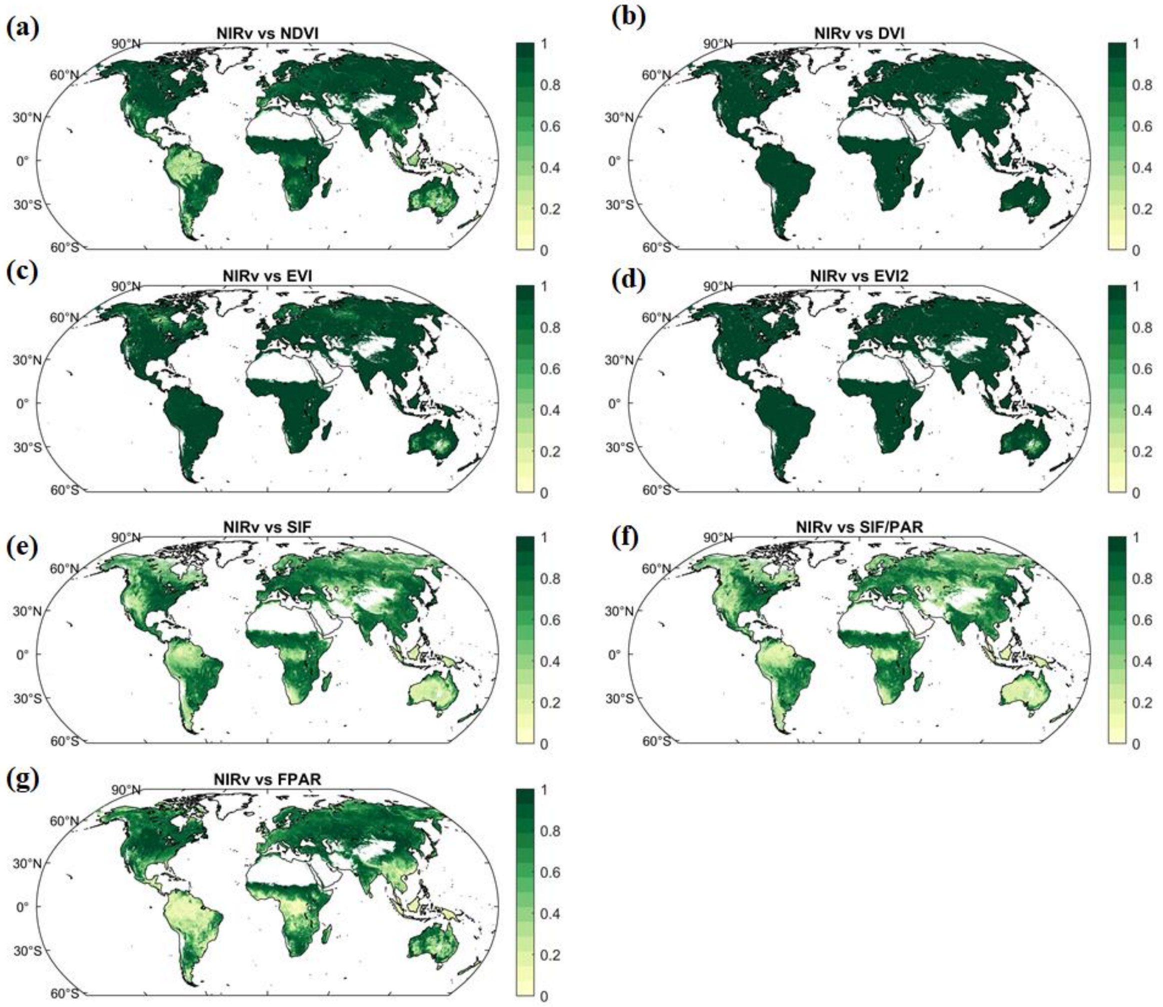

Fig. S3 Spatially-explicit temporal correlations between MODIS NIRv and other remote sensing measures. The dataset is during March 2018 to February 2019, with the temporal resolution of 4 days and 0.1° spatial resolution. The *R* between NIRv and DVI, EVI and EVI2 could be close to 1, in most places in the world (Fig. S3b-d). Among DVI, EVI and EVI2, the *R* between DVI and NIRv was the highest (Fig. 3b), followed by that between EVI2 and NIRv, with some exceptions in the arid/semiarid regions in central Australia. The *R* for EVI and NIRv was relatively smaller than that of DVI and EVI2 at high latitudes, possibly due to the noise in the blue band. The desirable effects of blue band on EVI is diminished over snow/ice, at the annual scale, as opposed to the growing season. This could be due to snow/ice contamination in more than 50% vegetated pixels. Global average *R* between NIRv and NDVI was about 0.87, but could be low (<0.3) over South American and Southeast Asian tropical rainforests as well as central Australian drylands. Global average *R* between NIRv and SIF was around 0.63, with the highest values (>0.8) primarily for places that were dominated by croplands or woody savannas. The *R* between NIRv and FPAR was relatively larger in the Northern Hemisphere than in the Southern Hemisphere, except for the forested area in low latitudes such as South China and Southeast Asia.

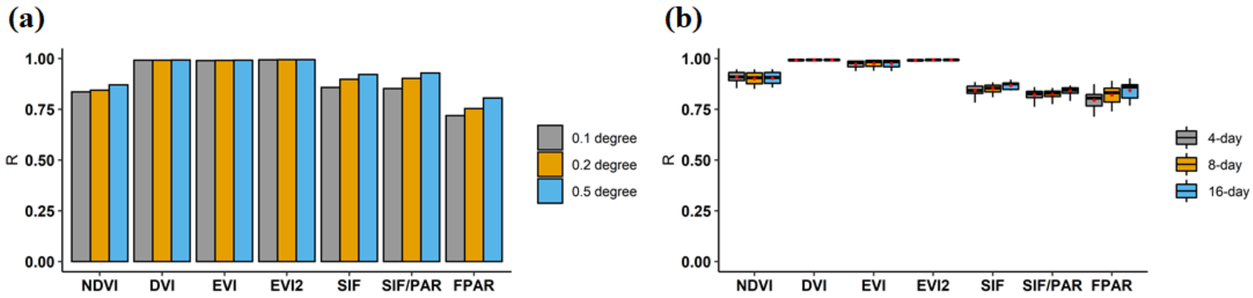

Fig. S4 Global spatial correlations between monthly-averaged MODIS NIRv and other remote sensing measures. The dataset was aggregated to different spatial resolutions (0.1° to 0.2° and 0.5°) in August, 2018 (panel **a**), during 2018.03-2019.02 period, upscaled to different temporal scales (4-, 8- and 16-day) and at 0.1° spatial resolution (panel **b**). Red circle refers to the mean value, boxes represent the interquartile ranges of the 25th (Q25) and 75th (Q75) percentiles, and whiskers cover the ranges of Q25 -1.5·(Q75 - Q25) and Q75+1.5·(Q75 - Q25). At 0.1° resolution, the spatial correlation (indicated by *R*) between NIRv and DVI, EVI or EVI2 was very high (*R*≈1), but relatively lower for NDVI, SIF, SIF/PAR and FPAR (*R*=0.84, 0.86, 0.85, and 0.72, respectively), respectively. *R* values for all indices increased with an increase in length of spatial window, except that *R* values for DVI, EVI and EVI2 were already very high. The temporal variation of 4-, 8- and 16-day DVI and EVI2 were highly correlated with NIRv (*R*≈1 almost everywhere). Spatial correlation between NIRv and EVI were also high across different temporal scales: all the periods had *R*>0.94.

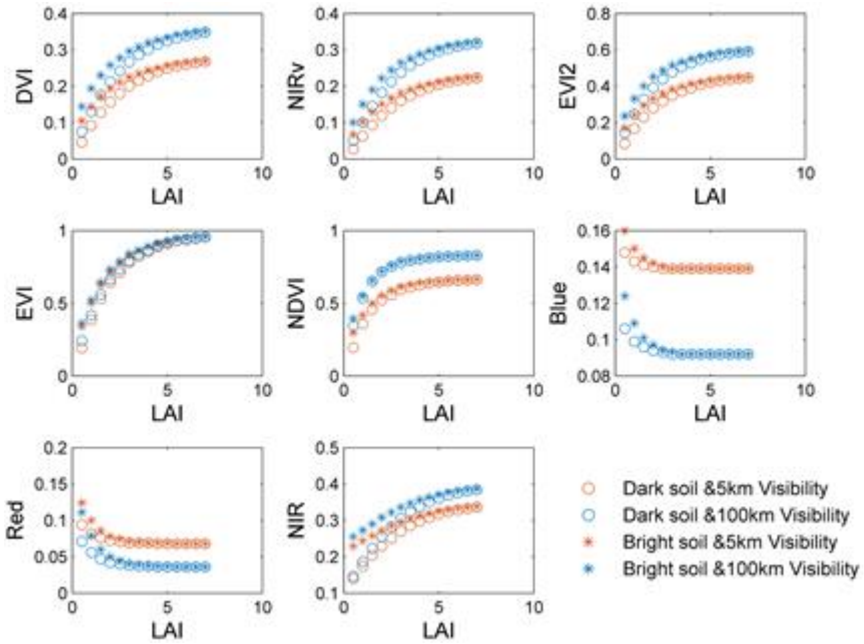

Fig. S5 Sensitivity analysis of different VIs and spectral bands. The dataset is at the top of atmosphere, under different atmospheric conditions (5-km visibility vs. 100-km visibility) and soil background (dark vs. bright). The atmospheric model type is mid-latitude summer, and the standard aerosol model is continental. Based on model simulations with Cab=60 μg cm^{-2}; spherical leaf inclination angle distribution; solar zenith angle=30°; nadir view; the LAI ranges from 0.5 to 7.0 with the step of 0.5. The canopy parameters are the same as Fig. S1. The top-of-atmosphere (TOA) NIRv, DVI and EVI2, with only the Red and NIR bands, have similar sensitivity to atmospheric conditions and soil background. For the same LAI, the atmospheric visibility has a larger impact on these VIs than soil background. The NDVI for TOA observations was sensitive to the atmospheric conditions, and shows sensitivities to soil background only when LAI is small, i.e., less than 1. The bright soil and dark soil have two different spectra shapes, and thus the bright soil with a steep slope of the reflectance spectrum happens to have a larger NDVI than the dark soil, while the bright soil usually has a smaller NDVI than the dark soil if the slope of the spectrum at the red edge is the same or flatter (Eq. 5). This means bright soil may not necessarily have a smaller NDVI than dark soil, and the slope of the spectrum at the red edge needs to be considered. EVI stands out to be the least impacted VI to either the atmospheric or soil background at all LAIs, with the introduction of the blue band into its formula. The coefficients of 6 and 7.5 in the denominator of EVI in Eq. 3 are for the aerosol effects, which uses the blue band to correct for the aerosol influences in the red band. Therefore EVI is recommended for use under imperfect atmospheric correction conditions.

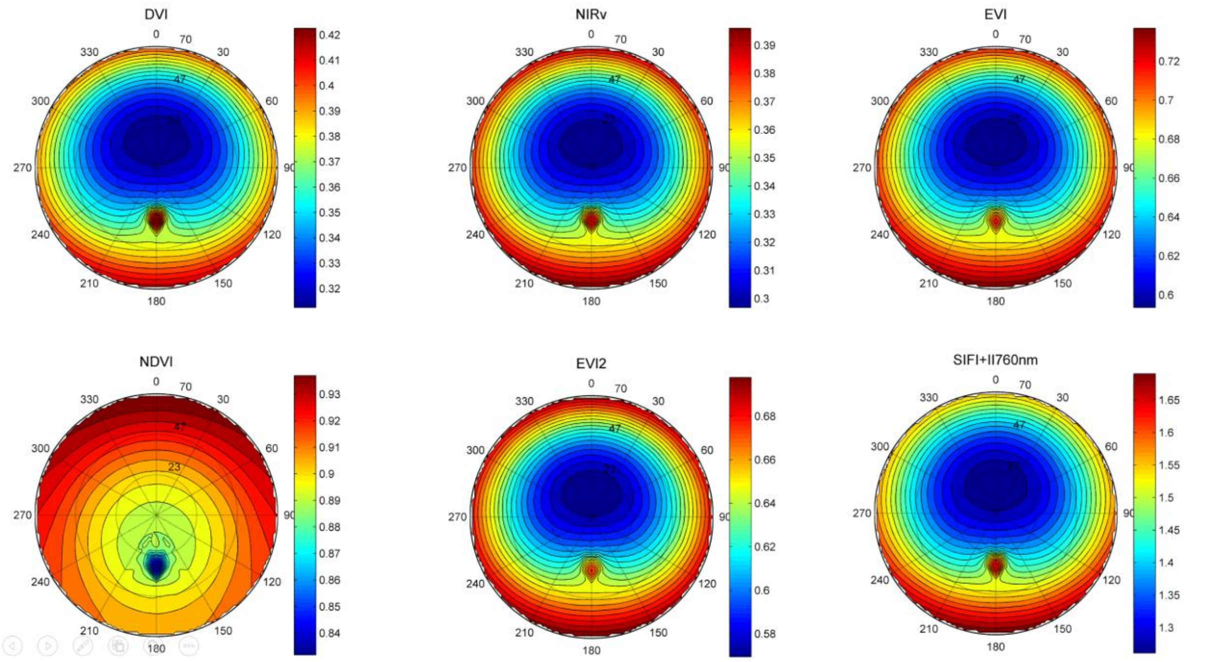

Fig. S6 The angular distribution of different VIs and SIF simulated by the SCOPE v1.70 model. The simulation dataset was set for LAI=3; Cab=60 μg cm^{-2}; spherical leaf inclination angle distribution; solar zenith angle=30°; the view zenith angle ranges from 0° to 70°. Except for NDVI, all the other four VIs and SIF have extremely similar hemispheric distributions with view angle. The maximum values are located in the hotspot direction where the sun and view angle coincide, while the values were the smallest in the forward scattering direction (dark-spot[23]) (Fig. S6a-c,e,f). In contrast, NDVI reached the minimum value for the hotspot, and the maximum value for the dark-spot (Fig. S6d). NDVI gradually became larger when the view angle was departing from the hotspot direction (more shadows) while the other VIs and SIF showed the opposite trends, except for large view zenith angles. This means NDVI responds differently to changes in the viewing geometry, and the shadows in view, from the other VIs and SIF. The variation of NDVI due to different view geometries was about 10% of its nadir value, while the variations of other indices were about 30% of their nadir values, suggesting that NDVI is less sensitive to the view geometry and the shadows in view than the other indices.

References

1 Serbin, S. P. *et al.* Remotely estimating photosynthetic capacity, and its response to temperature, in vegetation canopies using imaging spectroscopy. *Remote Sensing of Environment* **167**, 78-87 (2015).

2 Serbin, S. P. *et al.* UW-BNL NASA HyspIRI Airborne Campaign Leaf and Canopy Spectra and Trait Data. Data set. Available on-line at https://ecosis.org/package/uw-bnl-nasa-hyspiri-airborne-campaign-leaf-and-canopy-spectra-and-trait-data. *Ecological Spectral Information System (EcoSIS)* (2019).

3 Schaaf, C. B. *et al.* First operational BRDF, albedo nadir reflectance products from MODIS. *Remote sensing of Environment* **83**, 135-148 (2002).

4 Myneni, R. *et al.* Global products of vegetation leaf area and fraction absorbed PAR from year one of MODIS data. *Remote Sensing of Environment* **83**, 214-231 (2002).

5 Friedl, M. A. *et al.* Global land cover mapping from MODIS: algorithms and early results. *Remote Sensing of Environment* **83**, 287-302 (2002).

6 Gorelick, N. *et al.* Google Earth Engine: Planetary-scale geospatial analysis for everyone. *Remote sensing of Environment* **202**, 18-27 (2017).

7 Köhler, P. *et al.* Global retrievals of solar‐induced chlorophyll fluorescence with TROPOMI: First results and intersensor comparison to OCO‐2. *Geophysical Research Letters* **45**, 10,456-410,463 (2018).

8 Hao, D. *et al.* DSCOVR/EPIC-derived global hourly and daily downward shortwave and photosynthetically active radiation data at 0.1°× 0.1° resolution. *Earth System Science Data* **12**, 2209-2221 (2020).

9 Hao, D. *et al.* Estimating hourly land surface downward shortwave and photosynthetically active radiation from DSCOVR/EPIC observations. *Remote Sensing of Environment* **232**, 111320 (2019).

10 Van der Tol, C., Verhoef, W., Timmermans, J., Verhoef, A. & Su, Z. An integrated model of soil-canopy spectral radiances, photosynthesis, fluorescence, temperature and energy balance. *Biogeosciences* **6**, 3109-3129 (2009).

11 Vermote, E. F., Tanré, D., Deuze, J.-L., Herman, M. & Morcette, J.-J. Second simulation of the satellite signal in the solar spectrum, 6S: An overview. *Geoscience and Remote Sensing, IEEE Transactions on* **35**, 675-686 (1997).

12 Zeng, Y. *et al.* A practical approach for estimating the escape ratio of near-infrared solar-induced chlorophyll fluorescence. *Remote Sensing of Environment* **232**, 111209 (2019).

13 Hinojo-Hinojo, C. & Goulden, M. L. Plant traits help explain the tight relationship between vegetation indices and gross primary production. *Remote Sensing* **12**, 1405 (2020).

14 Turner, A. J. *et al.* A double peak in the seasonality of California's photosynthesis as observed from space. *Biogeosciences* **17**, 405-422 (2020).

15 Huete, A. R. A soil-adjusted vegetation index (SAVI). *Remote sensing of environment* **25**, 295-309 (1988).

16 Huete, A. *et al.* Overview of the radiometric and biophysical performance of the MODIS vegetation indices. *Remote Sensing of Environment* **83**, 195-213, doi:http://dx.doi.org/10.1016/S0034-4257(02)00096-2 (2002).

17 Liu, H. Q. & Huete, A. A feedback based modification of the NDVI to minimize canopy background and atmospheric noise. *IEEE transactions on geoscience and remote sensing* **33**, 457-465 (1995).

18 Qi, J., Chehbouni, A., Huete, A. R., Kerr, Y. H. & Sorooshian, S. A modified soil adjusted vegetation index. *Remote sensing of environment* **48**, 119-126 (1994).

19 Miura, T., Huete, A., Van Leeuwen, W. & Didan, K. Vegetation detection through smoke‐filled AVIRIS images: An assessment using MODIS band passes. *Journal of Geophysical Research: Atmospheres* **103**, 32001-32011 (1998).

20 Nagol, J. R., Vermote, E. F. & Prince, S. D. Effects of atmospheric variation on AVHRR NDVI data. *Remote Sensing of Environment* **113**, 392-397 (2009).

21 Vermote, E. & Vermeulen, A. Atmospheric correction algorithm: spectral reflectances (MOD09). *ATBD version* **4**, 1-107 (1999).

22 Jackson, R. D. & Huete, A. R. Interpreting vegetation indices. *Preventive veterinary medicine* **11**, 185-200 (1991).

23 Chen, J. M., Menges, C. H. & Leblanc, S. G. Global mapping of foliage clumping index using multi-angular satellite data. *Remote Sensing of Environment* **97**, 447-457, doi:10.1016/j.rse.2005.05.003 (2005).

24 Kaufmann, R. K. *et al.* Effect of orbital drift and sensor changes on the time series of AVHRR vegetation index data. *IEEE Transactions on Geoscience and Remote Sensing* **38**, 2584-2597 (2000).

25 Fensholt, R., Sandholt, I., Proud, S. R., Stisen, S. & Rasmussen, M. O. Assessment of MODIS sun-sensor geometry variations effect on observed NDVI using MSG SEVIRI geostationary data. *International Journal of Remote Sensing* **31**, 6163-6187 (2010).

26 Petri, C. A. & Galvão, L. S. Sensitivity of seven MODIS vegetation indices to BRDF effects during the Amazonian dry season. *Remote sensing* **11**, 1650 (2019).

27 Chen, J. M. Evaluation of vegetation indices and a modified simple ratio for boreal applications. *Canadian Journal of Remote Sensing* **22**, 229-242 (1996).

28 Beck, H. E. *et al.* Global evaluation of four AVHRR–NDVI data sets: Intercomparison and assessment against Landsat imagery. *Remote Sensing of Environment* **115**, 2547-2563 (2011).

29 Damm, A. *et al.* Impact of varying irradiance on vegetation indices and chlorophyll fluorescence derived from spectroscopy data. *Remote Sensing of Environment* **156**, 202-215 (2015).

30 Hilker, T. *et al.* Separating physiologically and directionally induced changes in PRI using BRDF models. *Remote Sensing of Environment* **112**, 2777-2788 (2008).

31 Galvão, L. S., Breunig, F. M., dos Santos, J. R. & de Moura, Y. M. View-illumination effects on hyperspectral vegetation indices in the Amazonian tropical forest. *International Journal of Applied Earth Observation and Geoinformation* **21**, 291-300 (2013).

32 Wang, Z., Schaaf, C. B., Sun, Q., Shuai, Y. & Román, M. O. Capturing rapid land surface dynamics with Collection V006 MODIS BRDF/NBAR/Albedo (MCD43) products. *Remote sensing of environment* **207**, 50-64 (2018).